

ARTICLE OPEN



Josephson detection of time-reversal symmetry broken superconductivity in SnTe nanowires

C. J. Trimble^{1,7}, M. T. Wei^{1,7}, N. F. Q. Yuan², S. S. Kalantre¹, P. Liu^{3,4}, H.-J. Han^{3,4}, M.-G. Han⁵, Y. Zhu⁵, J. J. Cha^{3,4,6}, L. Fu² and J. R. Williams¹✉

A Josephson junction (JJ) couples the supercurrent flowing between two weakly linked superconductors to the phase difference between them via a current-phase relation (CPR). While a sinusoidal CPR is expected for conventional junctions with insulating weak links, devices made from some exotic materials may give rise to unconventional CPRs and unusual Josephson effects. In this work, we present such a case: we investigate the proximity-induced superconductivity in SnTe nanowires by incorporating them as weak links in JJs and observe a deviation from the standard CPR. We report on indications of an unexpected breaking of time-reversal symmetry in these devices, detailing the unconventional characteristics that reveal this behavior. These include an asymmetric critical current in the DC Josephson effect, a prominent second harmonic in the AC Josephson effect, and a magnetic diffraction pattern with a minimum in critical current at zero magnetic field. The analysis examines how multiband effects and the experimentally visualized ferroelectric domain walls give rise to this behavior, giving insight into the Josephson effect in materials that possess ferroelectricity and/or multiband superconductivity.

npj Quantum Materials (2021)6:61; <https://doi.org/10.1038/s41535-021-00359-w>

INTRODUCTION

A Josephson junction (JJ) is a device where two superconductors are coupled by an insulating barrier, superconducting constriction, or conducting a weak link. Fundamental to these junctions is the relationship between the supercurrent (I_S) and the phase difference (ϕ) between the two superconductors, known as the current-phase relation (CPR)¹. For conventional JJs, this relationship is given by $I_S(\phi) = I_C \sin(\phi)$ where I_C is the critical current. Built into this CPR is a statement of time-reversal symmetry, which is reflected in the antisymmetric property $I_S(\phi) = -I_S(-\phi)$ of the CPR¹. The CPR can become more complex, for example in JJs with weak links made of high electrical quality materials. In these JJs, higher order processes arising from multiple Andreev reflections can add higher harmonics to the CPR. Despite the complexity, time-reversal symmetry in these junctions holds.

JJs have also been created with superconductors or weak links which possess broken time-reversal symmetry (BTRS). These systems include JJs with ferromagnetic weak links^{2,3} and with spin-orbit coupled materials in the presence of a magnetic field^{4–6}. This also includes materials that maintain time-reversal symmetry in the normal state but break this symmetry upon entering the superconducting state, including multicomponent superconducting states in multiband materials^{7,8}, grain boundaries in d-wave superconductors^{9,10} and in topological p-wave superconductors like Sr₂RuO₄¹¹. Junctions comprised of these materials exhibit common characteristics that arise from BTRS. The first is a measured critical current that depends on the sign of the current through the junction. The second is a CPR which is dominated by a second harmonic, a result of either the presence of transport channels that are out of phase—so-called “0” and “ π ” supercurrent channels—or a Josephson coupling that vanishes in the first order. This asymmetric critical current and dominant second harmonic

have been predicted and/or measured in JJs with materials containing ferromagnetism^{2,3,12–15} or spin-orbit interaction in the presence of a magnetic field^{16,17}, d-wave superconductors⁹, multiband superconductors^{18–23}, and topological (p-wave) superconductors^{24–27}.

Below we detail signatures of BTRS in JJs with SnTe nanowires, focusing on a critical current that depends on the direction of current flow and a strong second harmonic in the CPR. These JJs share many of the properties of aforementioned exotic superconducting junctions. We demonstrate how the combined effect of the multiple bands present at the Fermi energy and the existence of ferroelectric domain walls in SnTe can explain the two signatures of BTRS in these JJs. This multiband superconductivity and the new Josephson effects can be used to investigate a host of unconventional superconductivity properties including fractional vortices^{28,29}, topological superconductivity in multiband materials^{30–32}, and new types of Josephson-based devices in proximity-induced multiband and ferroelectric superconductors^{7,8}.

RESULTS

Broken symmetry in the DC Josephson effect

The Josephson effect is measured in JJs fabricated with SnTe nanowires using lock-in detection of the differential resistance $r = dV/dI$ as a function of the applied DC current (I_{DC}) and AC current (measured in power P) at a temperature of $T \sim 25$ mK (see Materials and Methods for further details on nanowire synthesis and measurement). $r(I_{DC})$ at $P = 0$ is shown in Fig. 1a. There is no dependence of $r(I_{DC})$ on the direction of the current sweep, indicating that the junction is overdamped³³. Unlike conventional overdamped JJs, different values of I_C are observed for positive (I_C^+) and negative (I_C^-) I_{DC} . Sweeps of I_{DC} in both directions reveal

¹Joint Quantum Institute and Quantum Materials Center, Department of Physics, University of Maryland, College Park, MD, USA. ²Department of Physics, Massachusetts Institute of Technology, Cambridge, MA, USA. ³Department of Mechanical Engineering and Materials Science, Yale University, New Haven, CT, USA. ⁴Energy Sciences Institute, Yale West Campus, West Haven, CT, USA. ⁵Department of Condensed Matter Physics and Materials Science, Brookhaven National Laboratory, Upton, NY, USA. ⁶Canadian Institute for Advanced Research Azrieli Global Scholar, Toronto, ON, Canada. ⁷These authors contributed equally: C.J. Trimble, M.T. Wei. ✉email: jwilliams@physics.umd.edu

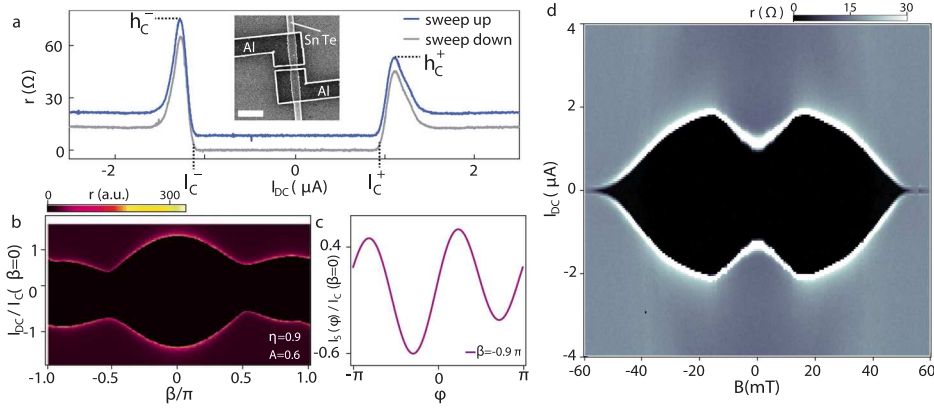


Fig. 1 The DC Josephson effect. **a** Differential resistance r as a function of DC bias current I_{DC} in different sweep directions. The bias sweeps show no hysteresis and two nonidentical critical currents and peak heights h_C^+ and h_C^- . The curves are offset for clarity. Inset: Schematic of a JJ consisting of two aluminum (Al) superconductors coupled via a SnTe nanowire. White scale bar is $1 \mu\text{m}$. **b** The simulated differential resistance $r(I_{DC}, \beta)$ calculated by the resistively shunted junction model, where the best fit of parameters (A, β) are $(0.6, -0.9\pi)$. The resulting CPR is plotted in **c**. **d** The magnetic diffraction pattern $r(I_{DC}, B)$, showing a critical current minimum at $B = 0$.

that the difference in I_C^+ and I_C^- remains. The measured critical currents $I_C^- = 1.1 \mu\text{A}$ and $I_C^+ = 0.92 \mu\text{A}$ give the critical current asymmetry $I_C^-/I_C^+ \approx 1.2$. These sweep-direction-invariant effects are not predicted for conventional JJs³³. Further, we also measure an asymmetric height of the peak in r , with the peak in r larger for I_C^- . The measured peak heights $h_C^- = 65.9 \Omega$ and $h_C^+ = 45.2 \Omega$ produce the peak height asymmetry $h_C^-/h_C^+ \approx 1.46$.

Numerical simulations of the resistively shunted junction model³⁴ were performed (Fig. 1b) to reveal the CPR that gives rise to this asymmetric critical current. Conventional JJs possess a CPR that is both inversion and π -translation antisymmetric, a result of time-reversal symmetry. The only way to reproduce $r(I_{DC})$ curves that are not symmetric in I_{DC} is to break both of these symmetries: we accomplish this with the CPR $I_S = I_C[(\sin(\phi) + \eta \sin(2\phi)) + A[\sin(\phi + \beta) + \eta \sin(2(\phi + \beta))]]$. This CPR is comprised of two terms, each containing a first and second harmonic, that is offset by a phase β . The parameter A determines the relative strength of the two terms in the CPR. The parameter η is the strength of the second harmonic terms that are expected to provide a significant contribution in the BTRS state for multiband materials^{21,22}. The presence of a strong second harmonic will be confirmed in our measurement of the AC Josephson effect (Fig. 2) and a value of $\eta = 0.9$ is extracted from these measurements. Values for A and β are chosen to best match the experimentally determined asymmetries $I_C^-/I_C^+ \approx 1.2$ and $h_C^-/h_C^+ \approx 1.46$ ³⁴: $A = 0.6$, $\beta = -0.9\pi$. The CPR for these values are shown in Fig. 1c and possesses BTRS, i.e., $I(\phi) \neq -I(-\phi)$. The essential features of these CPRs are the two inequivalent minima/maxima which occur at different values of I_S : it is these features that give rise to the differences in I_C^+ , I_C^- and h_C^+ , h_C^- .

Strong half-steps in the AC Josephson effect

JJs of SnTe show two other signatures of BTRS: a predominant second harmonic in the AC Josephson effect and a magnetic diffraction pattern with a minimum at zero magnetic field, as shown in Fig. 1d. We leave the detailed discussion of the diffraction pattern to ref. ³⁴, and now turn our attention to the modification of the AC Josephson effect. The presence of a second harmonic component—expected in the BTRS state^{21,22}—will result in additional steps at values of half the expected $hf/2e$. A plot of $r(I_{DC}, P)$ is shown in Fig. 2a taken at $f = 5 \text{ GHz}$. In addition to dips in r observed at the expected integer values (labeled in white), prominent features at half-integer values are also apparent. This is more clearly seen in cuts of Fig. 2a, shown in Fig. 2b taken at $P = -11.8 \text{ dBm}$. In addition to the dips in r (gray curve) at integer values, clear dips at half-integer values occur. In fact, the

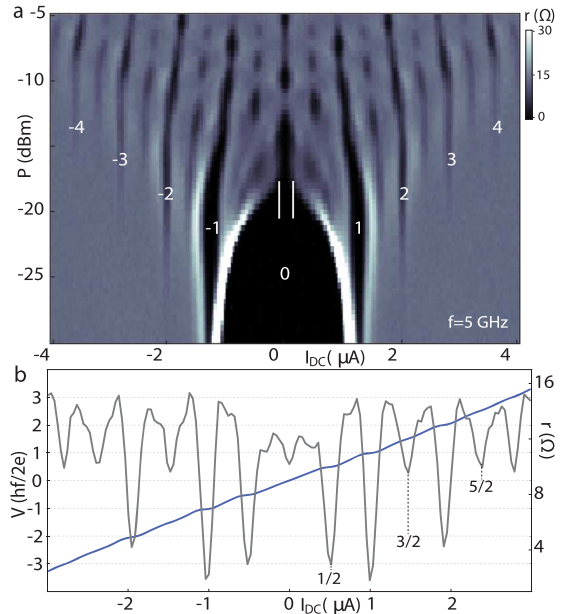


Fig. 2 AC Josephson effect. **a** In addition to the integer Shapiro steps, labeled in white, fractional Shapiro steps appear in between the integer ones in a plot of $r(I_{DC}, P)$. **b** $r(I_{DC})$ (gray curve) and integrated voltage $V(I_{DC})$ (blue curve) taken at an applied RF frequency $f = 5 \text{ GHz}$, $P = -11.8 \text{ dBm}$. The first 1/2 integer step occurs with nearly equal intensity to the first integer step.

drop in r at 1/2 is nearly equal to that at 1. In addition, the integrated voltage $V = \int (dV/dI) dI$ versus I_{DC} curve is shown in blue. The dips/plateaus measured in r/V are nearly equal in strength, indicating that the contributions of the first and second harmonic to the CPR are approximately equal. This depth magnitude is used to extract the value of $\eta = 0.9$ for the CPR used in the numerical simulations in Fig. 1b.

The Shapiro diagram (Fig. 2a) also has two other signatures that indicate nearly equal contributions from the first and second harmonic terms. First, the width of the zeroth step does not go to zero (indicated by the two white vertical lines), as expected for the zeroth-order Bessel function. It does go to zero for the second closure. Second, while the step width in I_{DC} of the half-integer steps is modulated with P , showing regions of P where the step width goes to zero (as is expected), the width modulation is less pronounced on the integer steps. These differences occur when

the CPR has both first and second harmonic terms (as detailed by simulations in ref. ³⁴).

Subharmonic steps are expected for underdamped junctions and for overdamped junctions with skewed CPR. Our junctions are overdamped; hence we rule out the former as being the cause. Skewed CPRs in overdamped junctions produce fractional Shapiro steps, but the strength of these steps is much reduced compared with the integer steps. For comparison, see ref. ³⁵ for the AC Josephson effect in a similar material, $\text{Pb}_{0.5}\text{Sn}_{0.5}\text{Te}$. The CPR in ref. ³⁵ used to reproduce the experimental data is that of a ballistic JJ, a CPR that has the greatest amount of skewness amongst the likely candidate CPRs. Yet, it produces dips at fractional values that are an order of magnitude smaller than the integer value dips. Therefore, we also rule out the skewed CPR as the source of the observed effect.

Multiband effect and ferroelectric distortion in SnTe

SnTe is not known to possess ferromagnetic correlations. It has a strong spin-orbit coupling but the effects observed in this paper are at zero magnetic field. Thus, Zeeman splitting or the effects of spin-orbit coupling in magnetic fields cannot explain our observation. Although SnTe is a topological crystalline insulator, as-grown SnTe nanowires have a Fermi energy buried in the valence^{36,37}; hence, transport properties should be dominated by the bulk electronic states. Doped via Sn vacancies, superconducting SnTe has properties that agree well with BCS theory. Yet it has been shown that multiband effects are essential in the description of superconductivity in this material³⁸.

In this work, superconductivity arises via the proximity effect, which has a very different character when the proximitized material has multiple bands. Nanowires of SnTe(100) have a rock salt structure that produces two effective bands in the electronic structure of SnTe³⁴. Figure 3a shows an illustration of the proximity effect at the interface between a material with two bands and the aluminum superconductor, where superconducting correlations are introduced into each band via couplings J_1 and J_2 . In addition, coupling between the bands J facilitated by scattering must also be taken into account. When all three couplings are present, the superconducting phase on each band can become unequal. It is at this interface and under the influence of these three couplings that time-reversal symmetry is broken (see ref. ³⁴ for a complete theoretical description).

The proximity effect between an s -wave superconductor and a multiband material shares similarities with a junction between an s -wave superconductor and an s_{\pm} superconductor. Theoretical investigations of junctions between s -wave and s_{\pm} superconductors demonstrate BTRS^{8,18,19}. The manifestation of BTRS is twofold. First is the creation of a canted state (Fig. 3d)^{18–21}, where a nonzero angle forms between the phase of the bands and the phase of the superconductor. Three possible phase angle configurations are shown: for $J \ll (J_1, J_2)$ (Fig. 3b), $J \gg (J_1, J_2)$ (Fig. 3c) and $J \sim (J_1, J_2)$ (Fig. 3d). In the case where $J \gg (J_1, J_2)$ and $J \sim (J_1 = J_2)$, a novel superconducting state called s_{\pm} is formed. The resulting effect of this canting is the generation of chiral currents in momentum space^{18,19}—a result of the Josephson currents produced by the difference in phase angle between different bands—that give rise to BTRS.

The results of the above references cannot, however, completely describe the experimental results of this Letter. A key distinction from those references is that the curve in Fig. 1c has two minima occurring at different values of I_S . These unequal minima are key to replicating the experimental results. Previous theoretical predictions dictate that these two minima be equal, a result of the two-phase angle configurations in Fig. 3d being time-reversal-symmetric partners¹⁹. Here, the low-temperature ferroelectric distortion has an important role, both in creating unequal magnitude in the phase angles in the two bands and the phase

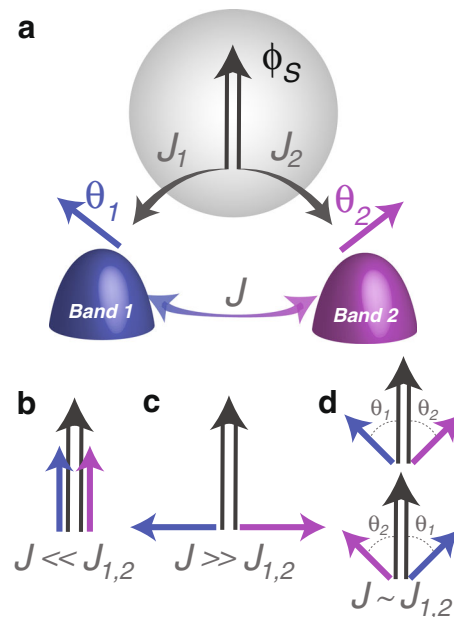


Fig. 3 Proximity effect in a two-band system. **a** The two bands in SnTe are coupled to the order parameter with phase ϕ_S in aluminum via an external pairing field for J_1, J_2 . The interband coupling J is facilitated by the scattering of carriers between bands. θ_1 and θ_2 are the phases of individual order parameters in the two bands. **b–d** The competition between the coupling strengths J and $J_{1,2}$ results in different relative phases between two bands. **b** When $J \ll J_{1,2}$, the phases tend to align with each other. **c** When $J \gg J_{1,2}$, the phases of two bands are out of phase by π . **d** In the intermediate regime $J \sim J_{1,2}$, the phases are canted (shown for the case $J_1 = J_2$). The two degenerate states in the BTRS case are shown.

accumulated by an electron/hole when crossing a domain wall between different ferroelectric domains.

The phase angles in the canted state are determined by the coupling to the Al superconductor ($J_{1,2}$), which is in part determined by the density of states at the Fermi energy in the SnTe nanowire. Bulk and thin-film SnTe are known to undergo a ferroelectric transition at low temperatures, causing an unequal density of states at the Fermi energy in the two bands of SnTe^{39,40}. Transport measurements of the SnTe nanowires have shown clear kinks in the resistivity curves as a function of temperature, indicative of the ferroelectric transition³⁶. However, the ferroelectric distortion has not been directly observed in nanowires. This is important to establish since the ferroelectric distortion will produce an unequal density of states in each band. The density of states in each band after the ferroelectric distortion can be estimated from the electronic density n . Although the electronic density n cannot be extracted from Hall measurements on nanowires, we can get an estimation for n from 2D platelets of SnTe grown under similar conditions, giving a value of $\sim 10^{21} \text{ cm}^{-3}$ ^{36,37}. This gives a Fermi energy of 330 meV. The ferroelectric distortion pushes one valence band down in energy by 300 meV⁴⁰ and both bands are occupied with a relative density of states size of approximately three between the large and small pocket.

To confirm the presence of a ferroelectric distortion, the SnTe nanowires were cooled down to 12 K in situ cryo-transmission electron microscope (TEM) experiments to visualize the ferroelectric transition and the microstructure of the ferroelectric domains present in the SnTe nanowires at low temperature (further TEM details can be found in ref. ³⁴). At room temperature, the SnTe nanowire shows uniform contrast in the bright-field TEM image (Fig. 4a); at 12 K, dark bands appear along the nanowire perpendicular to the long axis (Fig. 4b), which were absent at room temperature. These dark bands mark the domain walls

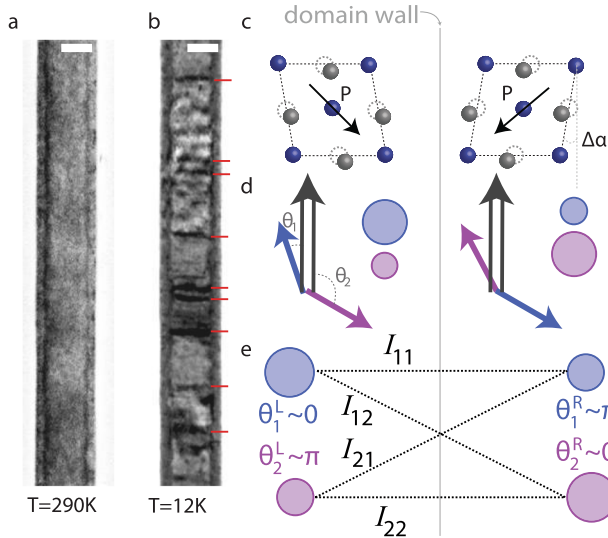


Fig. 4 Effect of ferroelectric distortion on proximity effect and Josephson current. **a–b** TEM images of a SnTe nanowire at $T = 290$ K and $T = 12$ K, respectively. The scale bar in the upper right corner of each image is 50 nm. Dark bands perpendicular to the growth direction, indicated by red lines in **b**, are domain walls separating different polarization directions. Scale bars in the upper right corner of each image are 50 nm. **c** The cubic lattice at room temperature undergoes a transition to a rhombohedral lattice at $T = 80$ K with two domains. **d** Unequal phase angles for the two ferroelectric domains. **e** The four-channel supercurrent flow across a domain wall. The two interband channels I_{ij} behave like conventional "0"-junctions, whereas the intraband channels I_{ii} behave like " π "-junctions.

between two ferroelectric domains that emerge at low temperatures. This was confirmed by examining the electron diffraction pattern from the nanowire. The ferroelectric transition is accompanied by the cubic-to-rhombohedral structural transition in SnTe. As the nanowire is cooled, the cubic electron diffraction at room temperature changes to show two sets of diffraction patterns that are rotated by an angle of $\Delta\alpha \sim 1.2^\circ$ ³⁴, consistent with the two expected ferroelectric domains (Fig. 4c). The cubic-to-rhombohedral phase transition occurs at 80 K for this nanowire, as all the dark bands suddenly disappear at this temperature³⁴.

The domain walls observed in Fig. 4a are important when considering the supercurrent flow through the JJ. Domain walls between superconducting order parameters are known to cause modifications to Josephson currents. For example, complete destruction of the magnetic diffraction pattern has been ascribed to the coexistence of many energetically degenerate p-wave superconducting domains¹¹. Also, the motion of the walls between different metastable positions can produce a fluctuating critical current^{41–43}. In some SnTe devices, we observe a similar fluctuation of critical current³⁴. Hence, we now consider the CPR across a domain wall in SnTe JJs.

DISCUSSION

The CPR can be calculated using the phase angles determined by the proximity effect. Across the domain wall will be four superconducting channels: two intraband and two interband channels^{8,19}. The four calculated CPRs are $I_{ij}(\phi) = i_{ij} \sin(\phi + \theta_j^R - \theta_i^L)$ for all pairs of $i, j = 1, 2$, where $\theta_{i(j)}^{L(R)}$ are the phase angles of the i th(j)th band on the left(right) side of the domain wall and $i_{ij} = 2eh\Delta_i^L\Delta_j^R/m$ ³⁴. Two conclusions can be drawn from a density of states that differs by a factor of approximately three on the two valleys. First, the valley with the larger pocket will have a phase

angle near zero, whereas the smaller pocket is near π ^{20,21}. Hence, $\theta_1^L, \theta_2^R \sim 0$ and $\theta_2^L, \theta_1^R \sim \pi$ (Fig. 4d), giving rise to two "0" interband ($i \neq j$) and two π intraband ($i = j$) supercurrent channels (Fig. 4e)^{8,19}. The presence of competing 0 and π channels explains the predominant second harmonic and the magnetic diffraction pattern. Further, we can use the density of states to estimate the magnitude proximity-induced superconducting gaps $\Delta_{1,2}^{L,R} = 3\Delta_{2,1}^{R,L} \equiv 3\Delta_0$. The relative magnitude of the "0" and " π " is then: $i_{12} + i_{21} = 2eh/m(\Delta_1^L\Delta_2^R + \Delta_2^L\Delta_1^R) = 2eh/m(10\Delta_0)$ and $i_{11} + i_{22} = 2eh/m(\Delta_1^L\Delta_1^R + \Delta_2^L\Delta_2^R) = 2eh/m(6\Delta_0)$. The ratio is 0.6. Both the phase and the relative amplitude agree very well with the values for A and β obtained from the simulation.

In summary, we have investigated the combined effects of proximity-induced multiband superconductivity and ferroelectric distortion on the dynamic properties of JJs with SnTe nanowire weak links. Four unexpected JJ behaviors—the asymmetric critical currents, peaks heights, strong second harmonic, and anomalous magnetic diffraction pattern—were explained within the theoretical framework. The role of the ferroelectric distortion offers new routes to control the flow of supercurrents, where modification of the density of states or ferroelectric transition temperature by electric fields and strain can be used to modulate the supercurrent and the offset phase in the device. The manifestation of multiband and multicomponent superconductivity in our devices offers experimental access to the phase induced on individual bands. This allows for the investigation of the order parameter in novel superconductors^{7,8} and for the determination of topology in the superconducting state^{30–32}.

METHODS

Nanowire growth

The SnTe nanowires measured in this study were synthesized by metal-catalyzed chemical vapor deposition using a single-zone furnace. SiO_2/Si substrates decorated with 20 nm-wide gold nanoparticles were used as growth substrates. SnTe and Sn source powders were mixed and placed at the center of a horizontal quartz tube with one-inch diameter while the growth substrates were placed upstream in the quartz tube, 10–13 cm away from the center. The furnace was heated to 600°C and remained at the temperature for 1 hr with an Ar carrier gas at a flow rate of 20 s.c.c.m. After the growth, the furnace was allowed to cool naturally. The growth substrates contain SnTe microcrystals, nanoplates, and nanowires whose atomic structure and chemical composition were characterized by TEM and energy-dispersive X-ray spectroscopy. The details of the synthesis reactions and microcharacterizations of SnTe nanowires can be found in our previous reports (Supplementary reference [5]). For this study, we select SnTe nanowires with cross-sectional lengths of $< \sim 300$ nm.

TEM

The nanowires were characterized by TEM for their atomic structure as well as chemical composition. The experiments were carried out using Gatan's liquid-He cryo holder (HCTDT 3010) and JEOL JEM-ARM200CF at 200 kV at Brookhaven National Laboratory. SnTe nanowires were drop-casted onto Cu-mesh TEM grids overlaid with a thin carbon support film. The TEM sample was cooled from room temperature to 12 K by cooling the cryo holder with liquid helium. The temperature sensor measures the temperature of the holder, and the actual temperature of the sample may be ~ 5 –10 K higher. More details about the cryo-TEM experiments are presented in ref.³⁴.

Device fabrication

Our Josephson devices are fabricated on ~ 5 mm \times 5 mm Si/SiO₂ chips with SnTe nanowires dispersed atop them. First, a pattern of equally spaced alignment marks is written using Elionix ELS-G100 100 kV Electron-Beam Lithography System with a dose of 1600 $\mu\text{C}/\text{cm}^2$. After the 60 s in situ argon plasma etch at 50 W, Ti/Au are deposited (5 nm/70 nm) using e-beam evaporation. After liftoff of the alignment marks, ideal SnTe wires are selected using an optical microscope. Then, the Josephson devices are written atop these wires using a dose of 1600 $\mu\text{C}/\text{cm}^2$. The sample undergoes a 60 s in situ argon plasma etch at 50 W, followed by the

sputtering of Ti/Al (4.5 nm/200 nm). An essential part of getting samples with measurable supercurrents at base temperature is the heating of the sample during the deposition of aluminum. During the deposition of aluminum, the sample is heated to 100°C.

Electrical measurements

Low-temperature transport measurements are carried out in dilution refrigerators with electron temperatures of <50 mK. DC electrical leads are heavily filtered to remove high-frequency noise above 10 kHz. Lock-in measurements are carried out using a 1 nA excitation at 13 Hz. Radiofrequency radiation up to 7 GHz is supplied to one of the electrical leads via a synthesizer through a bias-tee located on the chip carrier.

DATA AVAILABILITY

The data that support the findings of this study are available from the corresponding author upon reasonable request.

Received: 9 February 2021; Accepted: 25 May 2021;

Published online: 18 June 2021

REFERENCES

- Golubov, A. A., Kupriyanov, M. Y. & Il'ichev, E. The current-phase relation in Josephson junctions. *Rev. Mod. Phys.* **76**, 411–469 (2004).
- Sellier, H., Baraduc, C., Lefloch, F. & Calemczuk, R. Half-integer Shapiro steps at the $0 - \pi$ crossover of a ferromagnetic Josephson junction. *Phys. Rev. Lett.* **92**, 257005 (2004).
- Sickingler, H. Experimental evidence of a φ Josephson Junction. *Phys. Rev. Lett.* **109**, 107002 (2012).
- Ke, C. T. Ballistic superconductivity and tunable $\pi - \pi$ junctions in InSb quantum wells. *Nat. Comm.* **10**, 3764 (2019).
- Mayer, W. Gate controlled anomalous phase shift in Al/InAs Josephson junctions. *Nat. Comm.* **11**, 212 (2020).
- Schönle, J. Field-tunable $0 - \pi$ transitions in SnTe topological crystalline insulator SQUIDs. *Sci. Rep.* **9**, 1987 (2019).
- Tanaka, Y. Multicomponent superconductivity based on multiband superconductors. *Supercond. Sci. Technol.* **28**, 034002 (2015).
- Yerin, Y. & Omelyanchouk, A. N. Proximity and Josephson effects in microstructures based on multiband superconductors. *Low. Temp. Phys.* **43**, 1013–1037 (2017).
- Tanaka, Y. & Kashiwaya, S. Theory of Josephson effects in anisotropic superconductors. *Phys. Rev. B* **56**, 892–912 (1997).
- Il'ichev, E. et al. Degenerate ground state in a mesoscopic $\text{YBa}_2\text{Cu}_3\text{O}_{7-x}$ grain boundary Josephson junction. *Phys. Rev. Lett.* **86**, 5369–5372 (2001).
- Kidwingira, F., Strand, J. D., Van Harlingen, D. J. & Maeno, Y. Dynamical superconducting order parameter domains in Sr_2RuO_4 . *Science* **314**, 1267–1271 (2006).
- Goldobin, E., Koelle, D., Kleiner, R. & Buzdin, A. Josephson junctions with second harmonic in the current-phase relation: Properties of φ junctions. *Phys. Rev. B* **76**, 224523 (2007).
- Frolov, S. et al. Josephson interferometry and Shapiro step measurements of superconductor-ferromagnet-superconductor $0 - \pi$ junctions. *Phys. Rev. B* **74**, 020503(R) (2006).
- Moshe, M. & Mints, R. G. Shapiro steps in Josephson junctions with alternating critical current density. *Phys. Rev. B* **76**, 054518 (2007).
- Li, F. et al. Measurement of the intrinsic higher harmonic current-phase relation in NbN/NiCu/NbN Josephson junctions. *Phys. Rev. B* **99**, 100506(R) (2019).
- Reynoso, A. A. et al. Spin-orbit-induced chirality of Andreev states in Josephson junctions. *Phys. Rev. B* **86**, 214519 (2012).
- Yokoyama, T., Eto, M. & Nazarov, Y. V. Anomalous Josephson effect induced by spin-orbit interaction and Zeeman effect in semiconductor nanowires. *Phys. Rev. B* **89**, 195407 (2014).
- Ng, T. K. & Nagaosa, N. Broken time-reversal symmetry in Josephson junction involving two-band superconductors. *EPL* **87**, 17003 (2009).
- Lin, S.-Z. Josephson effect between a two-band superconductor with $s + +$ or $s \pm$ pairing symmetry and a conventional s -wave superconductor. *Phys. Rev. B* **86**, 014510 (2012).
- Stanev, V. G. & Koshelev, A. E. Anomalous proximity effects at the interface of s - and $s \pm$ -superconductors. *Phys. Rev. B* **86**, 174515 (2012).
- Koshelev, A. E. Phase diagram of Josephson junction between s and $s \pm$ superconductors in the dirty limit. *Phys. Rev. B* **86**, 214502 (2012).
- Sperstad, I. B., Linder, J. & Sudbø, A. Quantum transport in ballistic $s \pm$ -wave superconductors with interband coupling: Conductance spectra, crossed Andreev reflection, and Josephson current. *Phys. Rev. B* **80**, 144507 (2009).
- Huang, Z. & Hu, X. Josephson effects in three-band superconductors with broken time-reversal symmetry. *Appl. Phys. Lett.* **104**, 162602 (2014).
- Asano, Y., Tanaka, Y., Sigrist, M. & Kashiwaya, S. Josephson current in s -wave-superconductor/ Sr_2RuO_4 junctions. *Phys. Rev. B* **67**, 184505 (2003).
- Asano, Y., Tanaka, Y., Sigrist, M. & Kashiwaya, S. Josephson interferometer in a ring topology as a proof of the symmetry of Sr_2RuO_4 . *Phys. Rev. B* **71**, 214501 (2005).
- Nakamura, T. et al. Topological competition of superconductivity in Pb/Ru/ Sr_2RuO_4 junctions. *Phys. Rev. B* **84**, 060512(R) (2011).
- Anwar, M. S. et al. Multicomponent order parameter superconductivity of Sr_2RuO_4 revealed by topological junctions. *Phys. Rev. B* **95**, 224509 (2017).
- Chen, C.-T. et al. Integer and half-integer flux-quantum transitions in a niobium-iron pnictide loop. *Nat. Phys.* **6**, 260–264 (2010).
- Tanaka, Y. et al. Experimental formation of a fractional vortex in a superconducting bi-layer. *Phys. C Supercond. Appl.* **548**, 44–49 (2018).
- Qi, X.-L., Hughes, T. L. & Zhang, S.-C. Topological invariants for the Fermi surface of a time-reversal-invariant superconductor. *Phys. Rev. B* **81**, 134508 (2010).
- Hosur, P., Dai, X., Fang, Z. & Qi, X.-L. Time-reversal-invariant topological superconductivity in doped Weyl semimetals. *Phys. Rev. B* **90**, 045130 (2014).
- Guguchia, Z. et al. Signatures of the topological s^{++} superconducting order parameter in the type-II Weyl semimetal $\text{T}_d\text{-MoTe}_2$. *Nat. Comm.* **8**, 1082 (2017).
- Barone, A. & Paternò, G. *Physics and Applications of the Josephson Effect*. (Wiley-Interscience Publications, 1982).
- Details on the calculations and further experimental data can be found in the supplementary information.
- Snyder, R. et al. Weak-link Josephson junctions made from topological crystalline insulators. *Phys. Rev. Lett.* **121**, 097701 (2018).
- Shen, J. et al. Synthesis of SnTe nanoplates with {100} and {111} surfaces. *Nano Lett.* **14**, 4183–4188 (2014).
- Shen, J., Xie, Y. & Cha, J. J. Revealing surface states in In-doped SnTe nanoplates with low bulk mobility. *Nano Lett.* **15**, 3827–3832 (2015).
- Allen, P. B. & Cohen, M. L. Carrier-concentration-dependent superconductivity in SnTe and GeTe. *Phys. Rev.* **177**, 704–706 (1969).
- Chang, K. et al. Discovery of robust in-plane ferroelectricity in atomic-thick SnTe. *Science* **353**, 274–278 (2016).
- Chang, K. et al. Standing waves induced by valley-mismatched domains in ferroelectric SnTe monolayers. *Phys. Rev. Lett.* **122**, 206402 (2019).
- Bouhon, A. & Sigrist, M. Influence of the domain walls on the Josephson effect in Sr_2RuO_4 . *N. J. Phys.* **12**, 043031 (2010).
- Kambara, H. et al. Anomalous transport through the p -wave superconducting channel in the 3-K phase of Sr_2RuO_4 . *Phys. Rev. Lett.* **101**, 267003 (2008).
- Anwar, M. S. et al. Anomalous switching in Nb/Ru/ Sr_2RuO_4 topological junctions by chiral domain wall motion. *Sci. Rep.* **3**, 2480 (2013).

ACKNOWLEDGEMENTS

Synthesis of narrow SnTe nanowires was supported by NSF 1743896. Transport characterizations of SnTe nanowires were supported by DOE DE-SC0014476. The cryo-TEM work was supported by the US DOE Basic Energy Sciences, Materials Sciences and Engineering Division under Contract No. DE-SC0012704. Transport measurements of the JJ devices were sponsored by the grants National Science Foundation A "Quantum Leap" Demonstration of Topological Quantum Computing (DMR-1743913), Physics Frontier Center at the Joint Quantum Institute (PHY-1430094), and the Army Research Office Award W911NF-18-2-0075.

AUTHOR CONTRIBUTIONS

C.J.T. and M.T.W. contributed equally to this work. C.J.T. and M.T.W. performed the device fabrication and low-temperature Josephson measurements. P.L., H.-J.H., M.-G.H., Y.Z., and J.J.C. performed the cryo-TEM measurements. P.L. and H.-J. Han and J.J.C. performed the nanowire synthesis. N.F.Q. Yuan and L.F. provided theoretical calculations for the multiband proximity effect. M.T.W. and S.S.K. performed numerical simulations of the D.C. Josephson effect. All authors contributed to the writing of the manuscript.

COMPETING INTERESTS

The authors declare no competing interests.

ADDITIONAL INFORMATION

Supplementary information The online version contains supplementary material available at <https://doi.org/10.1038/s41535-021-00359-w>.

Correspondence and requests for materials should be addressed to J.R.W.

Reprints and permission information is available at <http://www.nature.com/reprints>

Publisher's note Springer Nature remains neutral with regard to jurisdictional claims in published maps and institutional affiliations.



Open Access This article is licensed under a Creative Commons Attribution 4.0 International License, which permits use, sharing, adaptation, distribution and reproduction in any medium or format, as long as you give appropriate credit to the original author(s) and the source, provide a link to the Creative Commons license, and indicate if changes were made. The images or other third party material in this article are included in the article's Creative Commons license, unless indicated otherwise in a credit line to the material. If material is not included in the article's Creative Commons license and your intended use is not permitted by statutory regulation or exceeds the permitted use, you will need to obtain permission directly from the copyright holder. To view a copy of this license, visit <http://creativecommons.org/licenses/by/4.0/>.

© The Author(s) 2021